

Transition mechanism of melt depth during Laser Powder Bed Fusion using in-situ X-ray and thermal imaging

Tomoya Ogura (✉ tmy289ogr11@akane.waseda.jp)

Waseda University - Nishiwaseda Campus: Waseda Daigaku - Nishiwaseda Campus

Yuki Wakai

National Institute of Advanced Industrial Science and Technology (AIST)

Shizuka Nakano

National Institute of Advanced Industrial Science and Technology (AIST)

Naoko Sato

National Institute of Advanced Industrial Science and Technology (AIST)

Satoshi Kajino

National Institute of Advanced Industrial Science and Technology (AIST)

Shinsuke Suzuki

Faculty of Science and Engineering, Waseda University

Research Article

Keywords: Additive manufacturing, Laser powder bed fusion, melting behavior, X-ray imaging, thermal imaging, recoil pressure

Posted Date: February 18th, 2021

DOI: <https://doi.org/10.21203/rs.3.rs-201819/v1>

License:   This work is licensed under a Creative Commons Attribution 4.0 International License.

[Read Full License](#)

Transition mechanism of melt depth during Laser Powder Bed Fusion using *in-situ* X-ray and thermal imaging

Tomoya Ogura¹, Yuki Wakai¹, Shizuka Nakano^{2*3},
Naoko Sato², Satoshi Kajino², Shinsuke Suzuki^{1*4*5},

*1 Department of Applied Mechanics and Aerospace Engineering,
Faculty of Science and Engineering,

Waseda University, 3-4-1 Okubo, Shinjuku, Tokyo 169-8555, Japan

*2 National Institute of Advanced Industrial Science and Technology (AIST),
1-2-1 Namiki, Tsukuba, Ibaraki 305-8564, Japan

*3 Henry Monitor Inc., 942-2 Shiga, Suwa, Nagano 392-0012, Japan

*4 Kagami Memorial Research Institute of Materials Science and Technology,
Waseda University, 2-8-16 Shinjuku, Tokyo 169-0051, Japan

*5 Department of Materials Science, Faculty of Science and Engineering,
Waseda University, 3-4-1 Okubo, Shinjuku, Tokyo 169-8555, Japan

Corresponding author : Tomoya Ogura,

tmy289ogr11@akane.waseda.jp, +81-3-5286-8126

Acknowledgments

This research was supported by Japan Science and Technology (JST),
under the Industrial-Academia Collaborative R&D Program

“Heterogeneous Structure Control: Towards Innovative Development of Metallic Structural
Materials”.

Abstract

This research clarified the transition mechanism of melt depth in Ti powder bed during Laser Powder Bed Fusion process using *in-situ* X-ray and thermal imaging. A fiber laser beam of 150 W was irradiated on a powder bed at a scan speed of 15 mm/s for 3.5 s in a vacuum chamber. The obtained X-ray images showed a keyhole depth L_d increased immediately after laser irradiation, gradually

decreased, and became constant. It also showed a keyhole width L_w increased immediately after laser irradiation and decreased afterward, after that, L_w increased again, and became constant. Furthermore, thermal images that measured the temperature on the powder bed showed the high temperature width L_h gradually increased and become constant. The model of the driving force which pushed the molten droplet was examined by analyzing the volume and scattering speed of the molten droplet. The model indicated the recoil pressure caused by the vaporization of powder metal was a driving force for the molten droplet scattering. The transition mechanism of keyhole depth was considered as follows. The increase of L_d at the beginning is due to the increase of the recoil pressure P_T . This is because the decrease of L_w and large quantity of vaporization. Next, the decrease of L_d is due to the decrease in P_T . This is because the increase of L_w and decrease of quantity of vaporization. At last, the transition to the constant L_d is caused by stabilization of L_w and L_h followed by stabilization of P_T .

(247 words)

keywords (4~6)

Additive manufacturing, Laser powder bed fusion, melting behavior, X-ray imaging, thermal imaging, recoil pressure

1. Introduction

Additive manufacturing (AM) is a processing technology that is available for manufacturing a hollow and complicated shape, so the further spread of AM is expected in the fields of aerospace [1], automobile [2], and medical [3]. Laser Powder Bed Fusion (LPBF) process, which is a kind of AM, is that a laser scans two-dimensionally and melts a thin layer of powder metal, which is repeated until a 3D shape is fabricated. Now, the rough surface in the product made by the LPBF process affects the drop of the mechanical properties, and additional machining processes to make the surface smooth would be required [4, 5]. Previous studies focused on the morphology of the single-track melt pool to clarify the cause of rough surface. Melt depth change affects surface roughness and the bonding between layers. A method to reduce internal defects and improve the surface property is to change the combination of processing parameters. However, it is difficult to find optimal processing condition from a combination of parameters in each material.

Melting behavior influences the relative density and surface property of the product. Therefore, Laser energy density (LED) is widely used for an index to find the most suitable processing condition. LED is expressed as the value that divides laser power by scanning speed, the thickness of the powder bed, and laser diameter [6]. Melting behavior changes by LED. For example, Prashanth *et al.* revealed that the relative density became 99% at high LED and tensile strength became large with high scan speed and large laser power at constant LED [7]. However, Promoppatum *et al.* revealed that melting

behavior was unstable when LED was superabundant. Although the relationship between LED and the final product has already been revealed, melting behavior between them is unexplained [8]. Therefore, *in-situ* observation is necessary to figure out the melting behavior in detail.

Previous study revealed that the characteristic melting behavior was observed using either X-ray or thermal imaging: balling [9], spatter [10-12], melt pool shape [13, 14], wettability [9], pore formation [13, 15], solidification [10], temperature distribution [16-18], keyhole [19]. Based on these, it is expected that the melting behavior in single-track examination can be clarified in detail by combining *in-situ* simultaneous observation of melting powder by X-ray imaging and temperature distribution measurement by thermal imaging. Then, our group established an analytical method using X-ray and thermal imaging simultaneously for the first time [20]. Wakai *et al.* classified the variations of the melting behavior with time at one-point irradiation using X-ray and thermal imaging. As a result, it became clear that a keyhole was formed just after irradiation start and the expansion of the keyhole depth is settled by the generation of the molten metal, and then molten metal rose by evaporation of powder metal.

Chimura *et al.* observed keyhole shape by *in-situ* X-ray imaging during laser welding [21]. Laser welding has a similar process to LPBF in terms of that a heat source is a laser and material is melted and solidified by the scanning of the laser continually. Chimura *et al.* revealed that keyhole depth increased as laser irradiation advanced and became constant before long. In welding, processing quality is known to be worse due to the molten droplet being scattered by the recoil pressure that occurred by evaporation of the metal, and it remains as a defect. The recoil pressure is the power that acts on the keyhole surface in opposite direction with the evaporation direction as a difference of the momentum when metal evaporated. Chimura *et al.* clarified that a keyhole was deepened with increasing recoil pressure.

About the two-dimensional melting of powder metal in LPBF, it was reported that the melt depth that is perpendicular to the scanning direction decreased [17]. It was supposed that this phenomenon was caused by the transition of the melting behavior from the melting form of local heating to the stable melting form. From this, about single-track analysis, it is supposed that the melt depth that is parallel to the scanning direction decreases based on a similar mechanism. However, the transition of melt depth itself has still been unexplained.

Recoil pressure was found to be proportional to the quantity of vaporization and inversely proportional to a vaporization area in a previous study on laser welding [21]. There is a difference between welding and LPBF, that is bulk materials are used in welding while powder metal is used in LPBF. In LPBF, the apparent density of powder bed is almost 60%. Therefore, it is supposed that the keyhole shape which is relevant to a vaporization area greatly changes when solidified bulk is formed and a void between the particles is integrated with a keyhole. Also, it is thought that as laser irradiation advances, powder metal around the irradiation point is heated and a sintered material is formed. After

that, the quantity of vaporization decreases as thermal diffusion promotes and recoil pressure decreases. Then, we conceived to acquire temperature distribution around the irradiation point using thermal imaging and observe the time change of keyhole using X-ray imaging. Based on these *in-situ* simultaneous observations, we can calculate recoil pressure quantitatively and elucidate relations with melt depth change.

The objective of this study is to clarify the transition mechanism of melt depth during single-track laser irradiation. During Ti powder was irradiated by laser beam, the high temperature width which is the area where the temperature of the powder rise and shape of the keyhole were measured by X-ray and thermal imaging. Besides, the relationship among high temperature width, keyhole shape, and the recoil pressure was discussed.

2. Materials and methods

2.1 Experimental Setup and materials

Figure 1 shows a schematic of LPBF experiments conducted in this study using *in-situ* X-ray and thermal imaging. The following parameters were different from those in our previous paper [20]: powder metal, the material of the container, its transferring method, laser irradiation condition, the X-ray tube voltage and current. Spherical pure Ti powder of average particle size under 45 μm (TILOP-45: OSAKA Titanium Technologies Co., Ltd.) which was produced by gas atomization method was used. Pure Ti was used because it is well used in AM and is easy to measure temperature due to clear melting point compared with Ti6Al4V. Table 1 shows the chemical composition of the powder described in the mill sheet provided by the supplier. The powder was placed into a rectangular sample container (130 mm long, 13 mm deep, 5 mm wide, 1 mm wall thickness) made of aluminum alloy A5052. The container was tapped 5 times to increase packing density. The powder bed was flattened using a ruler. The mass of the container with and without powder was measured and packing density α was calculated from those differences. As a result of calculation from Eq. (1), packing density α was estimated to be 58 %.

$$\alpha = \frac{M_p}{\rho_{\text{Ti}}V_S} \quad (1)$$

Here M_p is the mass of the powder, ρ_{Ti} the density of titanium, V_S the volume of the sample holder [22]. The specimen was placed inside a vacuum chamber made of stainless steel.

The fused-silica window was located on the top part of the vacuum chamber as a window for laser transmission and measurement by a two-color pyrometer. The pressure in the vacuum chamber became less than 6.8×10^{-2} Pa just after laser irradiation through evacuation by a turbo molecular pump (HiCube80Eco: Pfeiffer vacuum GmbH) connected to the vacuum chamber.

The single-mode fiber laser of the continuous-wave in Gaussian distribution (ASF1J256-R07P: Furukawa Electric Co., Ltd) was used as a heat source. The output of the laser was set based on a

beam profiling system (MaxTM LM – 100: Coherent. Inc). The laser beam entered at $q_i = 75^\circ$, relative to the powder bed surface, so as not to interfere with the two-color pyrometer. The distance from the laser beam to the irradiation point was about 200 mm. The container with the specimen was transferred linearly by a stepping motor (AZM46MC-TS10 : Oriental motor Co., Ltd.) as indicated by the arrow in Fig.1, and the laser beam was irradiated on the powder metal from the fixed laser and melted in a straight line. The experimental conditions included the laser power P of 150 W, the scan speed of $15 \text{ mm} \cdot \text{s}^{-1}$, and irradiation time t of 3.5 s.

During laser irradiation, the specimen was irradiated by an X-ray source (MTT255: Shimadzu Corp.) from the direction which was perpendicular to the scanning direction for *in-situ* observation of melting behavior. X-ray was irradiated through a Be-window (19 mm in diameter and 0.1 mm thick: Pascal Co., Ltd.). The Be-window was located at the entrance and exit of the vacuum chamber. X-ray reached a CCD camera finally. The X-ray tube voltage and current were set to 150 kV and 90 μA , respectively. The transmitted X-ray was converted to visible light using an image intensifier (IA9LM-10: Shimadzu Corp.). The images were recorded by a CCD camera (PCI2000S: NAC Image Technology, Inc.) with a resolution of 52 $\mu\text{m}/\text{pixel}$ and a frame rate of 500 fps.

During laser irradiation, the two-color pyrometer (Thermera - NIR: Mitsui Photonics Ltd.) with a 200-mm macro-lens (AIAF Micro-Nikkor ED 200 mm f/4D IF-ED: Nikon Corp.) measured the temperature distribution on the powder bed surface. The two-color pyrometer was set about 600 mm away from the surface of the powder bed, which enabled to observe all the width of the sample container is put in the visual field of the camera. The shooting conditions included a frame rate of 50 fps and exposure time of 0.1 s. The intensities of the two infrared wavelengths ($\lambda_1 = 800 \text{ nm}$ and $\lambda_2 = 975 \text{ nm}$) were measured as R_1 and R_2 , respectively. The temperature T was calculated from the ratio of these intensities using Eq. (2) which was derived from Planck's equation [23].

$$T = C_2 \times \left(\frac{1}{\lambda_1} - \frac{1}{\lambda_2} \right) \times \left\{ \frac{1}{\log\left(\frac{R_2}{R_1}\right)} - 5 \log\left(\frac{\lambda_1}{\lambda_2}\right) \right\} \quad (2)$$

Here $C_2 = 1.438759 \times 10^{-2} \text{ m} \cdot \text{K}$ is the second radiation constant, λ_n ($n = 1, 2$) is the wavelength of the emitted light, and R_n is the radiation intensity at wavelength λ_n . The size of the images was calculated to be 640×480 pixels with a pixel resolution of 13.3 μm . The exact size of the images was calculated from the width of sample holders, 3 mm. The black area of images expresses that the two-color pyrometer cannot measure both R_1 , R_2 intensity mainly because this kind of area is out of the temperature measuring range of the two-color pyrometer.

2.2 X-ray image processing

The obtained X-ray images were processed for analysis using software (Fiji) [24]. All the data were not binarized at the same brightness because the brightness of the outline of the keyhole changes as the laser scan advanced. At first, X-ray images were reversed horizontally to match the scan direction to the right. Second, median filter and Fast Fourier Transform (FFT) were applied to the raw X-ray images to remove an impulse noise and frequency component noise, respectively. Third, smooth filter was applied to the processed images. Finally, the contrast of the processed images was adjusted. Image processing included the following steps: i) median filter, ii) FFT, iii) smooth filter, iv) B/C contrast adjustment.

- i. median filter
- ii. FFT
- iii. smooth filter
- iv. B/C contrast adjustment

2.2.1 X-ray image quantification

After X-ray image processing, keyhole width L_w and keyhole depth L_d were measured as shown in Fig.2 using the algorithm made by python language. Keyhole means a hole that forms in the powder bed under the irradiation point.

1. Definition of a surface of the powder bed

For all images (1750 pictures) from irradiation start, the average brightness of the atmosphere and the powder bed were acquired each. the interface between atmosphere and powder bed was defined based on those average. After that, the value that was almost the arithmetical mean of two of them was defined as the surface of the powder bed. As a result, the surface of the powder bed pointed at the low side of the brightness. Therefore, the brightness that was about 5 high from the arithmetical mean was defined as the surface of the powder bed. The decision of the surface of the powder bed was done by sight.

2. Measurement of keyhole width L_w

- (i) X-ray image that the deepest part of the keyhole was easy to find as shown in Fig.5(b) at $t = 0.484$ s was chosen. A straight line at gun elevation 75° (laser irradiation angle) from the deepest part of the keyhole was drawn. At that time, the deepest part of the keyhole was decided by sight. The point of intersection of that line and the surface of the powder bed was defined as a laser irradiation point as shown in Fig.2(a). The surface of the powder bed defined after the keyhole formed was defined as a line that extended from the powder bed interface of the non-irradiation part.
- (ii) Keyhole width L_w was defined as the width of the keyhole under 15 pixels from the powder bed surface and measured as shown in Fig.2(b). Brightness 63 which was the most proper extraction of the outline of keyhole by sight was used.

3. Measurement of keyhole depth L_d

Keyhole depth L_d was defined as the length from the irradiation point to the point that the outline of the keyhole on a straight line at gun elevation 75° from the irradiation point as shown in Fig.2(b). Brightness 55 was used from irradiation start to 0.7 s and Brightness 60 was used from 0.7 s to 3.5 s, which was the most proper extraction of the outline of keyhole by sight.

4. Analysis of the spatter

Diameter r and velocity v of the molten droplets were measured using manual tracking of Fiji.

2.3 Thermal image processing and quantification

Thermal images were turned 180° to match the scan direction to the right. After thermal image processing, high temperature width L_h was measured as shown in Fig.3 using the following steps.

1. In thermal images, the point where the temperature was measured for the first time was decided as an irradiation point. Furthermore, the image that temperature was observed for the first time was defined as the irradiation start time (0 s) and synchronized with the X-ray image.
2. Point "A" was moved from irradiation point to y^+ axis and point "B" was moved from irradiation point to y^- axis, the point that the R strength became lower than 10 was defined as the edge of the high temperature area.
3. Time change of distance from point "A" to "B" was measured as high temperature width L_h .

3. Results

3.1 X-ray imaging

3.1.1 Analysis results of X-ray images

Figure 4 shows three examples of the obtained raw X-ray images. Figure 4(a) shows an X-ray image before laser irradiation start. The bright region on the upper side of the image is the atmosphere, and the dark region on the lower side of the image is the powder bed. Figure 4(b) shows the X-ray image during laser irradiation at $t = 0.430$ s. The slightly bright region compared with the powder and narrow region in the powder bed is the keyhole that was generated under the laser beam, which is often observed in the welding [21, 25]. The slightly dark region compared with the powder bed which existed behind the keyhole ($-x$ direction) is solidification bulk and molten droplet. The black and spherical object at the center of the X-ray image is a spatter. It was scattered above and fell again on the powder bed. Figure 4(c) shows the X-ray image during laser irradiation at $t = 2.088$ s. The black and spherical object on the right side of the solidification bulk is a molten droplet. The black region at the four corners of the X-ray image is the chamber that was reflected. The above fact was confirmed from thermal images later. These had already confirmed in our previous paper that used the same experimental equipment [20].

3.1.2 Time change of melting behavior

Figure 5 shows the melting behavior of the powder metal. Figure 5(a) shows the obtained raw X-ray images for observation of spatter. As a specific example, molten droplets named S1~S5 were picked up and showed a moving direction with an arrow. Figure 5(b) shows processed images whose minimum and maximum brightness were 40 and 120, respectively to focus on keyhole shape in a powder bed. Furthermore, Figure 5(c) shows the measurement result of the keyhole depth L_d and the keyhole width L_w . The circle on the straight line shows the edge of the keyhole, the distance of the interval is measured as keyhole depth and keyhole width.

Molten droplets S1 and S2 generated just after laser irradiation start were scattered in the direction (over the powder bed) of the arrow which was shown in Fig5(a). As laser irradiation advanced, molten droplets S3~5 formed right under an irradiation point moved to reverse with the scanning direction and jumped into solidification bulk as shown at $t = 1.680, 2.156, \text{ and } 3.226 \text{ s}$.

3.1.3 Time variation of the keyhole shape

Figure 6 shows the time variation of the keyhole width L_w and keyhole depth L_d which corresponds to the distances between two points in Fig5(c). The horizontal and the vertical axes express time and length, respectively. The points where the keyhole width was 0 mm were omitted due to the analysis error.

Keyhole depth L_d increased in the range of $t = 0 - \text{about } 0.4 \text{ s}$, gradually decreased in the range of $t = \text{about } 0.4 - 1.6 \text{ s}$ as laser scan advanced, and then became constant.

Keyhole width L_w increased just after irradiation start and decreased in the range of $t = \text{about } 0.1 - 0.4 \text{ s}$. After that, L_w increased again in range of $t = \text{about } 0.4 - 1.0 \text{ s}$, became constant finally. The cause of the increase and decrease of L_w after keyhole width became constant is the case that there is molten droplet right under an irradiation point as shown at $t = 3.214 \text{ s}$ in Fig.5(b) and the case after molten droplet jumped into solidification bulk as shown at $t = 2.226 \text{ s}$ in Fig.5(b). Also, L_d and L_w increased at the same speed just after the irradiation start.

3.1.4 Analysis of the molten droplets (spatter)

Figure 7 shows the trace and moving velocity of molten droplets S1 ~ S5 using manual tracking in Fiji. Each plot in the trace expresses the place where a molten droplet existed for each frame (every 0.002 s) which corresponds to the frame rate of 500 fps of the CCD camera. The moving velocity was calculated by dividing the moving distance by 0.002 s (1 frame).

The molten droplets formed just after irradiation start was scattered over the powder bed. As laser irradiation advanced and keyhole depth decreased, the molten droplets which were generated right under an irradiation point moved opposite to a scanning direction and jumped into solidification bulk. The maximum moving velocities were 147, 214, 257, 268 and 271 mm/s for S1, S2, S3, S4 and S5,

respectively. Although the moving direction was different from each other, the maximum velocity was almost at the same level. From this result, it was suggested that the same driving force acted at any time during laser irradiation.

3.2 Thermal imaging

3.2.1 Temperature distribution

Figure 8 shows the variation of the temperature distribution with time with the corresponding cross-sectional view of X-ray images during laser irradiation. All the thermal images showed that the temperature rose from the edge of the melt pool toward the irradiation point.

Figure 8(a) shows A, B, and irradiation point which were decided in chapter 2.3. The region which measured R intensity in fig.8(a) shows powder, molten droplet, and solidified bulk which performed a temperature rise to about 1300-2400°C that is the temperature measuring range of two-color pyrometer. Other parts are a vapor, Ti powder, and a sample container which were outside of the measuring temperature range. In this study, R intensity was used for analysis because it showed the edge of the temperature rise area clearly.

Compared with Figs.8(c) and (d), S1~S5 which were scattered over the powder bed and jumped into backward solidification bulk would be molten droplets because their temperature is close to the melting point of titanium 1668°C and their shape were spherical [22].

3.2.2 High temperature width L_h

Figure 9 shows the time variation of the high temperature width L_h , distance between A and B which was shown in Fig.8. Also, Fig.10 shows the thermal images which correspond to the three kinds of plots (black, red and light blue) shown in Fig.9. As shown in Figs.10(a) and (b), L_h is overestimated by the molten droplet which existed on the measurement line that is parallel to the y-axis through an irradiation point as shown at $t = 0.06$ s in Fig.8(a). In Fig.10(c) outline of the temperature rose area could not be extracted because temperature around the irradiation point could not be measured. Fig.10(d) is an example of the normal measurement. From these, only black plots that were measured exactly were linked in a line omitting red and light blue plots. As a result, L_h gradually increased as laser irradiation advances and became constant.

4. Discussion

In this chapter, the time when L_w , L_d and L_h became constant is defined using the coefficient of self-correlation. Besides, a model about the recoil pressure that pushed the molten droplets is constructed and this phenomenon is examined quantitatively. Based on these, the transition mechanism of melt depth is clarified by considering the relationship among the recoil pressure and each value of L_w , L_d and L_h .

4.1 Time variation of a keyhole shape and high temperature width

In terms of L_w and L_d in Fig.6, and L_h in Fig.9, the time when became constant was examined quantitatively. The correlation coefficient was counted backward from 3.5 s when laser irradiation finished and was calculated using the CORREL function of Microsoft Excel TM. The correlation coefficient is a statistical index indicating the correlation (the degree of similarity) between two random variables. It expresses the strength of the linear relations of two data in values of -1~1. Particularly, the coefficient of self-correlation was calculated because the data acquired in this study were chronological order data. In this study, when the coefficient of self-correlation deviated from the range of -0.2 - 0.2 for the first time, that time was defined as a constant value. Besides, for example, when two datum had the relationship of the trigonometric function (not linear), the correlation coefficient was a value close to 0. However, based on the assumption that L_w , L_d and L_h become constant (linear change) in this study, the coefficient of self-correlation was used for judgment of the constant value.

As a result, keyhole depth L_d became constant at $t = 1.812$ s as shown in Fig.6(a). L_w decreased temporarily and increased afterward at the peak which is shown in a circle in Fig.6(b). At the time of peak outbreak, following phenomena that L_w decreased because the molten droplet formed right under the irradiation point and L_w increased because the molten droplet jumped into backward solidification bulk as shown in X-ray images (at $t = 2.156, 3.226$ s) in Fig.5 was confirmed. After the consecutive datum with values less than 1.8 mm were omitted in the peaks shown in circles, the coefficient of self-correlation of L_w was calculated. As a result, keyhole width L_w became constant at $t = 1.298$ s as shown in Fig.6(b). The high temperature width L_h became constant at $t = 1.66$ s as shown in Fig.9. Here, only using the data which were measured normally, the coefficient of self-correlation was calculated.

When the above results were summarized, the time when became constant was keyhole width L_w , high temperature width L_h , and keyhole depth L_d in ascending order. It was suggested that the transition of L_d was affected by L_w and L_h .

4.2 A dynamic evaluation of the molten droplet and investigation of the driving force

Then, the driving force that pushed a scattered molten droplet from a volume and scattering speed of a molten droplet was examined. Figure 11 shows that a simple model of the movement of a molten droplet. It is supposed that the molten droplet was moved by the driving force F_d through the expansion of vapor from powder metal. Based on moving velocity v and the mass of molten droplet m calculated from its diameter, the driving force F_d which pushed a molten droplet was calculated. The driving force is expressed as the following Eq. (3) based on the expression of the impulse.

$$F_d = \frac{mv}{\Delta t} \quad (3)$$

Then, the driving force F_d was calculated through substitution of maximum velocity to v and substitution of the interval of record 0.002 s to Δt . Furthermore, Chimura *et al.* made a model of the recoil pressure that occurred by vaporization of metal [21]. From Eqs. (5) and (6), the recoil pressure was found to be inversely proportional to a vaporization area S and proportional to the quantity of vaporization rate \dot{m}_v .

$$v_t = \frac{1}{4} \sqrt{\frac{8kT_b}{\pi m_a}} \quad (4)$$

$$\dot{m}_v = \frac{P_v}{\Delta H_v} \quad (5)$$

$$P_t = \frac{\dot{m}_v V_t}{S} \quad (6)$$

$$F_v = \frac{V_t P_v}{\Delta H_v} \quad (7)$$

Here V_t is the vaporization velocity of the atom, k the Boltzmann constant, T_b the boiling point, m_a the atomic mass, P_v the laser power consumed for vaporization, ΔH_v the vaporization latent heat, S the vaporization area. The numerator on the right side of Eq. (6) expresses the theoretical value F_v of the volume expansion by the vaporization. Compared F_d with the vaporization F_v , it was able to be considered whether the driving force that pushed a molten droplet was due to the vaporization of powder metal or not. Here, \dot{m}_v was assumed to be constant and F_v was calculated. Laser power consumed for vaporization P_v was calculated based on the assumption that 20 % of all the laser output was absorbed [26]. Besides, Fig.12 shows F_d of S1~ S5 and the molten droplets which were observed except for S1~ S5.

As a result, vaporization F_v became larger than all F_d . Furthermore, the average of the early period of F_d became larger than that of the latter half of F_d . These results are examined in consideration of a temperature change in the next chapter.

4.3 Evaluation of melting behavior by thermal results

The results in Fig.12 were obtained without considering the time change of the quantity of vaporization rate \dot{m}_v accompanied with the temperature change around the irradiation point. It was revealed that L_h increased gradually in Fig.9 as laser irradiation advanced. It was suggested that as L_h increased, the temperature of the powder metal around the irradiation point rose and sintered material was formed. As a result, thermal diffusion was promoted and local heating was mitigated, and then laser power consumed for vaporization P_v decreased. Due to the occurrence of this phenomenon, the recoil pressure decreased as laser scan advanced. Thus, the theoretical value of vaporization F_v shown in Fig.12 was the smaller value when temperature change around the irradiation point was considered, and a relative error with the experimental value of vaporization F_v is shortened as shown in the

schematic in Fig.13.

In the first place, it is difficult to measure the driving force to push a molten droplet during irradiation accurately, but in this study, it was calculated experimentally. The experimental value F_d is not so far off by an order of magnitude compared to the theoretical value F_v . The experimental values F_d were calculated under the assumption that the scattering velocity was two-dimensional and not all the evaporated atoms contributed to the scattering. Therefore, the actual driving force F_d is expected to be larger than calculated values F_d . Therefore, from the results in this study and previous studies [10-12], it is reasonable to assume that the driving force to push a molten droplet was generated through the evaporation of the metal powder. If the F_d can be measured quantitatively, the keyhole depth at that time can be roughly estimated. This can be used as a guideline to set the irradiation conditions with fewer defects for industrial use.

4.4 The relationship among keyhole shape, high temperature width and recoil pressure

The recoil pressure was calculated by dividing driving force F_d by a vaporization area S calculated from keyhole shape. Then, the vaporization area was approximated as an elliptic cylinder. It was supposed that the elliptical semi-major axis is $\frac{L_w}{2}$ and semi-minor axis is $\frac{L_w}{4}$, and then the height is L_d . Figure 14 shows the relationship between the keyhole depth and the recoil pressure. The circle plot shows molten droplets which generated just after irradiation start, and the rhombus plot shows the molten droplets which generated after about 1.5 s. The tendency was showed that the keyhole depth increased with increasing the recoil pressure as shown in the previous study [21]. In Fig.14, the two plots at 60~65 Pa have small L_d despite the large recoil pressure. This can be attributed to the large recoil pressure due to the heating at the laser tip even before the keyhole depth becomes large. The two plots at 60-65 Pa correspond to the molten droplets generated at 0.010 s and 0.032 s. At that time, the keyhole was shallow and the powder metal was heated by the laser tip. It has been revealed that the vaporization rate was largest when the powder was heated by the laser tip immediately after the start of laser irradiation, and the keyhole deepens later than the increase of recoil pressure [21]. Therefore, it can be understood that a large recoil pressure pushed the molten droplet immediately after the start of laser irradiation and the keyhole deepened later than the increasing recoil pressure in this study. Also, two circle plots with L_d of 2.13 mm (23 Pa, 74 Pa) show another scattered molten droplet at the same time ($t = 0.052$ s). Normally, the same recoil pressure would push them. Therefore, it is conceivable that there are points with different recoil pressures even within the same keyhole depending on the multiple reflections of the laser in the keyhole.

Although the recoil pressure was calculated by the velocity of molten droplets, it is necessary to examine relations with the keyhole depth in the future by acquiring the quantity of vaporization by simulation. Furthermore, it turned out that heating form varied from local heating in the keyhole tip to heating in the surface of the keyhole wall by the multiple reflections of the laser beam as laser

irradiation advances [21]. Because it was thought that the recoil pressure decreased when this phenomenon occurred, the quantity of vaporization is an important examination item and is the point that cannot be considered in this study.

4.5 Transition mechanism of melt depth by single-track laser irradiation

Figure 15 shows a schematic of the transition mechanism of melt depth by single-track laser irradiation after $t = 0.13$ s. The transition mechanism of melt depth by single-track laser irradiation was thought as follows. The increase of L_d is seen early in irradiation, which is caused by the increase of the recoil pressure P_T due to the decrease of L_w and large quantity of evaporation m_v (small L_h). Next, the decrease of L_d is seen as laser scan advanced, which is caused by the decrease of the recoil pressure P_T due to the increase of L_w and decrease of quantity of evaporation m_v (an increase of L_h). At this point, the decrease in the quantity of evaporation can be attributed to the formation of the sintered material, which promotes thermal diffusion and reduces the laser power consumed for evaporation. In addition, the increase in L_w considered to be due to the formation of the solidified bulk, which makes the voids between the powder metal apparent and the keyhole apparent. Finally, the transition to the constant L_d is caused by stabilization of L_w and L_h followed by stabilization of P_T .

5. Conclusion

By *in-situ* simultaneous observation methods combining X-ray and thermal imaging, the following knowledge about the melting behavior of the powder bed during the LPBF process was obtained.

- 1) Keyhole depth L_d increased at first, gradually decreased as laser irradiation advanced, and then became constant finally. Keyhole width L_w increased just after irradiation start and decreased thereafter. After that, L_w increased again, became constant finally. High temperature width L_h gradually increased as laser irradiation advanced. The time when became constant was keyhole width L_w , high temperature width L_h and keyhole depth L_d in ascending order.
- 2) The transition mechanism of melt depth by single-track laser irradiation after $t = 1.3$ s was thought as follows. The increase of L_d in the early period of the irradiation is due to the increase of the recoil pressure P_T . This is because the decrease of L_w (decrease of vaporization area S) and large quantity of vaporization m_v (small L_h). Next, the decrease of L_d is due to the decrease of the recoil pressure P_T . This is because the increase of L_w and decrease of quantity of vaporization m_v (due to the increase of L_h). At last, the transition to the constant L_d is caused by stabilization of L_w and L_h followed by stabilization of P_T .

Declarations

-Ethical Approval

Not applicable.

-Consent to Participate

The authors declare that they all consent to participate this research.

-Consent to Publish

The authors declare that they all consent to publish the manuscript.

-Authors Contributions

Not applicable.

-Funding

Not applicable.

-Competing Interests

Not applicable.

-Availability of data and materials

All data generated or analysed during this study are included in this published article and its supplementary information files.

References

[1] Kasperovich G, Hausmann J (2015) Improvement of fatigue resistance and ductility of TiAl6V4 processed by selective laser melting. *J Mater Process Technol* 220:202–214.

<https://doi.org/10.1016/j.jmatprotec.2015.01.025>

[2] Böckin D, Tillman AM (2019) Environmental assessment of additive manufacturing in the automotive industry. *J Clean Prod* 226: 977–987. <https://doi.org/10.1016/j.jclepro.2019.04.086>

[3] Osakada K, Shiomi M (2006) Flexible manufacturing of metallic products by selective laser melting of powder. *Int J Mach Tools Manuf* 46:1188–1193.

<https://doi.org/10.1016/j.ijmachtools.2006.01.024>

[4] Liu Y, Yang Y, Mai S, Wang D, Song C (2015) Investigation into spatter behavior during selective laser melting of AISI 316L stainless steel powder. *Mater Des* 87:797–806.

<http://dx.doi.org/10.1016/j.matdes.2015.08.086>

[5] Song B, Dong S, Zhang B, Liao H, Coddet C (2012) Effects of processing parameters on microstructure and mechanical property of selective laser melted Ti6Al4V. *Mater Des* 35:120–125.

[10.1016/j.matdes.2011.09.051](https://doi.org/10.1016/j.matdes.2011.09.051)

- [6] Ciurana J, Hernandez L, Delgado J (2013) Energy density analysis on single tracks formed by selective laser melting with CoCrMo powder material. *Int J Adv Manuf Technol* 68:1103–1110. <https://doi.org/10.1007/s00170-013-4902-4>
- [7] Prashanth KG, Scudino S, Maity T, Das J, Eckert J (2017) Is the energy density a reliable parameter for materials synthesis by selective laser melting? *Mater Res Lett* 5:386–390. <https://doi.org/10.1080/21663831.2017.1299808>
- [8] Promopattum P, Onler R, Yao S (2017) Numerical and experimental investigations of micro and macro characteristics of direct metal laser sintered Ti-6Al-4V products. *J Mater Process Technol* 240:262–273. <http://dx.doi.org/10.1016/j.jmatprotec.2016.10.005>
- [9] Leung CLA, Marussi S, Towrie M, del Val Garcia J, Atwood RC, Bodey AJ, Jones JR, Withers PJ, Lee PD (2018) Laser-matter interactions in additive manufacturing of stainless steel SS316L and 13-93 bioactive glass revealed by in situ X-ray imaging. *Addit Manuf* 24:647–657. <https://doi.org/10.1016/j.addma.2018.08.025>
- [10] Zhao C, Fezzaa K, Cunningham RW, Wen H, de Carlo F, Chen L, Rollett AD, Sun T (2017) Real-time monitoring of laser powder bed fusion process using high-speed X-ray imaging and diffraction. *Sci Rep* 7:1–11. <https://doi.org/10.1038/s41598-017-03761-2>
- [11] Guo Q, Zhao C, Escano LI, Young Z, Xiong L, Fezzaa K, Everhart W, Brown B, Sun T, Chen L (2018) Transient dynamics of powder spattering in laser powder bed fusion additive manufacturing process revealed by in-situ high-speed high-energy x-ray imaging. *Acta Mater* 151:169–180. <https://doi.org/10.1016/j.actamat.2018.03.036>
- [12] Leung CLA, Marussi S, Atwood RC, Towrie M, Withers PJ, Lee PD (2018) In situ X-ray imaging of defect and molten pool dynamics in laser additive manufacturing. *Nat Commun* 9:1355. <https://doi.org/10.1038/s41467-018-03734-7>
- [13] Guo Q, Zhao C, Qu M, Xiong L, Hojjatzadeh SMH, Escano LI, Parab ND, Fezzaa K, Sun T, Chen L (2020) In-situ full-field mapping of melt flow dynamics in laser metal additive manufacturing. *Addit Manuf* 31:100939. <https://doi.org/10.1016/j.addma.2019.100939>
- [14] Cheng B, Lydon J, Cooper K, Cole V, Northrop P, Chou K (2018) Infrared thermal imaging for melt pool analysis in SLM: a feasibility investigation. *Virtual Phys Prototyp* 13:8–13. <https://doi.org/10.1080/17452759.2017.1392685>
- [15] Leung CLA, Marussi S, Towrie M, Atwood RC, Withers PJ, Lee PD (2019) The effect of powder oxidation on defect formation in laser additive manufacturing. *Acta Mater* 166:294–305. <https://doi.org/10.1016/j.actamat.2018.12.027>
- [16] Qiu C, Panwisawas C, Ward M, Basoalto HC, Brooks JW, Attallah MM (2015) On the role of melt flow into the surface structure and porosity development during selective laser melting. *Acta Mater* 96:72–79. <https://doi.org/10.1016/j.actamat.2015.06.004>
- [17] Yamamoto S, Azuma H, Suzuki S, Kajino S, Sato N, Okane T, Nakano S, Shimizu T (2019)

- Melting and solidification behavior of Ti-6Al-4V powder during selective laser melting. *Int J Adv Manuf Technol* 103:4433–4442. <https://doi.org/10.1007/s00170-019-03384-z>
- [18] Chivel Y, Smurov I (2010) On-line temperature monitoring in selective laser sintering/melting. *Physics Procedia* 5:515-521. doi:10.1016/j.phpro.2010.08.079
- [19] Zhirnov I, Protasov C, Kotoban D, Gusarov AV, Tarasova T (2017) New approach of true temperature restoration in optical diagnostics using IR-camera. *J Therm Spray Technol* 26:648–660. <https://doi.org/10.1007/s11666-017-0523-z>
- [20] Wakai Y, Ogura T, Nakano S, Sato N, Kajino S, Suzuki S (2020) Melting behavior in laser powder bed fusion revealed by in situ X-ray and thermal imaging. *Int J Adv Manuf Technol* 110:1047-1059. <https://doi.org/10.1007/s00170-020-05828-3>
- [21] Chimura I, Kawahito Y, Murakawa H (2016) Clarification of Keyhole Formation in Laser Welding of Stainless Steel with Particle Method and X-ray in-situ Observation. 23:145-152.
- [22] Lide DR, Frederikse HPR (1997) *CRC Handbook of Chemistry and Physics* 78th edition. CRC Press, Boca Ration.
- [23] Hottel HC, Broughton FP (1932) Determination of true temperature and total radiation from luminous gas flames. *Ind Eng Chem Anal Ed* 4:166-175.
- [24] Schneider CA, Rasband WS, Eliceiri KW (2012) NIH image to ImageJ: 25 years of image analysis. *Nat Methods* 9:671–675. <https://doi.org/10.1038/nmeth.2089>
- [25] Kawahito Y, Uemura Y, Doi Y, Muzutani M, Nishimoto K, Kawakami H, Tanaka M, Fujii H, Nakata K, Katayama S (2015) Elucidation of effect of welding speed on melt flows in high-brightness and high-power laser welding of stainless steel on basis of three-dimensional X-ray transmission in-situ observation. *Q J Jpn Weld Soc* 33:13-19.
- [26] Furumoto T, Ueda T, Hosokawa A, Abe S, Childs THC (2007) Study on the Measurement of Physical Properties in the Metal Powder for Rapid Prototyping -Proposal of the Measurement of Thermal Conductivity and Absorption of Laser Beam-. *Int J Jpn Soc Prec Eng* 73:558-562. <https://doi.org/10.2493/jjspe.73.558>

Figure caption list

(Figures were created by the programs, Microsoft Office Excel and PowerPoint)

Fig.1 Schematic of LPBF process experiments using X-ray and thermal imaging, and scanning manner.

Fig.2 Schematics of cross-sectional views of the powder bed. Definition of each reference point(a), just after laser irradiation start (b), and after generation of the melt track for the definition of measurement points L_w , L_d , v and r (c).

Fig.3 Schematic of the top view of the powder bed for the definition of the high temperature width L_h .

Fig.4 Examples of the obtained raw X-ray images before laser irradiation(a), during laser irradiation at $t = 0.430$ s (b), and during laser irradiation at $t = 2.088$ s (c).

Fig.5 Time change of melting behavior and definition of keyhole depth L_d and keyhole width L_w . Molten droplets named S1~S5 were examples that show characteristic melting behavior. Molten droplets S1 and S2 which were generated just after laser irradiation start were scattered at the direction of the arrow which was shown in Fig5(a). As laser irradiation advanced, molten droplets S3~5 formed right under an irradiation point moved to reverse with the scanning direction.

Fig.6 Time variation of keyhole depth L_d (a) and keyhole width L_w (b). The points where the keyhole width was 0 mm were omitted due to the analysis error. The dashed line shows the time when L_d and L_w became constant as shown in chapter 4.1. The circle shows the data which were omitted to calculate the correlation coefficient in chapter 4.1.

Fig.7 Trajectory (a) and velocity change (b) of molten droplets S1, S2, S3, S4 and S5 shown in Fig5(a). The arrow expresses a scattering direction (a).

Fig.8 Time change of temperature distribution from the top with corresponding X-ray images from the side. At $t = 0.06$ s in Fig.8(a), the symbols A and B express the edge of the temperature rise area (R intensity ≥ 10) on the straight line that is perpendicular to the x-axis through an irradiation point.

Fig.9 Time change of the high temperature width L_h . The dashed line shows the time when L_h became constant as shown in chapter 4.1. The red plots show that L_h is overestimated by the molten droplet which existed on the measurement line that is parallel to the y-axis through an irradiation point as shown in Figs.10(a) and (b). The light blue plots show that the outline of the temperature rose area could not be extracted because temperature around the irradiation point could not be measured as shown in Figs.10(c).

Fig.10 Example of thermal images at each time. The flame color of the images corresponds to the color of the plot in Fig.9. L_h is overestimated by the molten droplet which existed on the measurement line (a), (b). Outline of the temperature rose area could not be extracted because of not

measuring temperature around the irradiation point (c). The normal measurement (d)

Fig.11 Model of the spattering phenomenon for elucidating the driving force that pushed a molten droplet during the LPBF process.

Fig.12 Comparison of the driving force F_d that pushed a molten droplet and vaporization F_v . F_d is the driving force that pushed a molten droplet, F_v is the theoretical value of vaporization.

Fig.13 Comparison of the driving force F_d that pushed a molten droplet and vaporization F_v considering temperature change. The schematics that evaporation F_v decreased due to the decrease of quantity of vaporization \dot{m}_v as laser scan advanced. It was thought that as L_h increased, the temperature of the powder metal around the irradiation point rose and sintered material was produced. As a result, thermal diffusion was promoted and local heating was mitigated, and then the quantity of vaporization \dot{m}_v decreased. In addition, the result that the average of the early period of F_d became larger than that of the latter half of F_d was also considered because of the decrease of vaporization.

Fig.14 Relationship between the measured keyhole depth L_d and recoil pressure P_T . The recoil pressure was calculated by dividing driving force F_d as shown in Fig.13 by a vaporization area S calculated from keyhole shape at that time. The vaporization area was approximated as an elliptic cylinder. It was supposed that the elliptical semi-major axis is $\frac{L_w}{2}$ and semi-minor axis is $\frac{L_w}{4}$, and then the height is L_d . The kind of plot corresponds to Fig.13. The circle plots are the value that divided F_d of the early period of irradiation by a vaporization area S at that time. The rhombus plots are the value that divided F_d of the irradiation latter half by a vaporization area S at that time.

Fig.15 Schematic of the transition mechanism of melt depth by single-track laser irradiation. Keyhole depth L_d increased (a), decreased (b), and became constant (c) in time order. Quantity of vaporization rate \dot{m}_v increased immediately after irradiation start, decreased as the laser irradiation advanced, and transitioned to a constant value. The decrease in \dot{m}_v can be attributed to the formation of the sintered material, which promotes thermal diffusion and reduces the laser power consumed for evaporation. After $t = 0.13$ s, keyhole width L_w (vaporization area S) decreased once, then increased again and became constant. The increase in L_w considered to be due to the formation of the solidified bulk, which makes the voids between the powder metal apparent. It is assumed that the recoil pressure P_T which is expressed as the ratio of these two parameters (\dot{m}_v and S) increased after the start of laser irradiation, gradually decreased as laser irradiation advanced and then became constant. Due to the causes mentioned above, L_d is thought to have caused the same changes as

recoil pressure.

Table 1 Chemical composition of Ti powder used in this study (mass %)

Figures

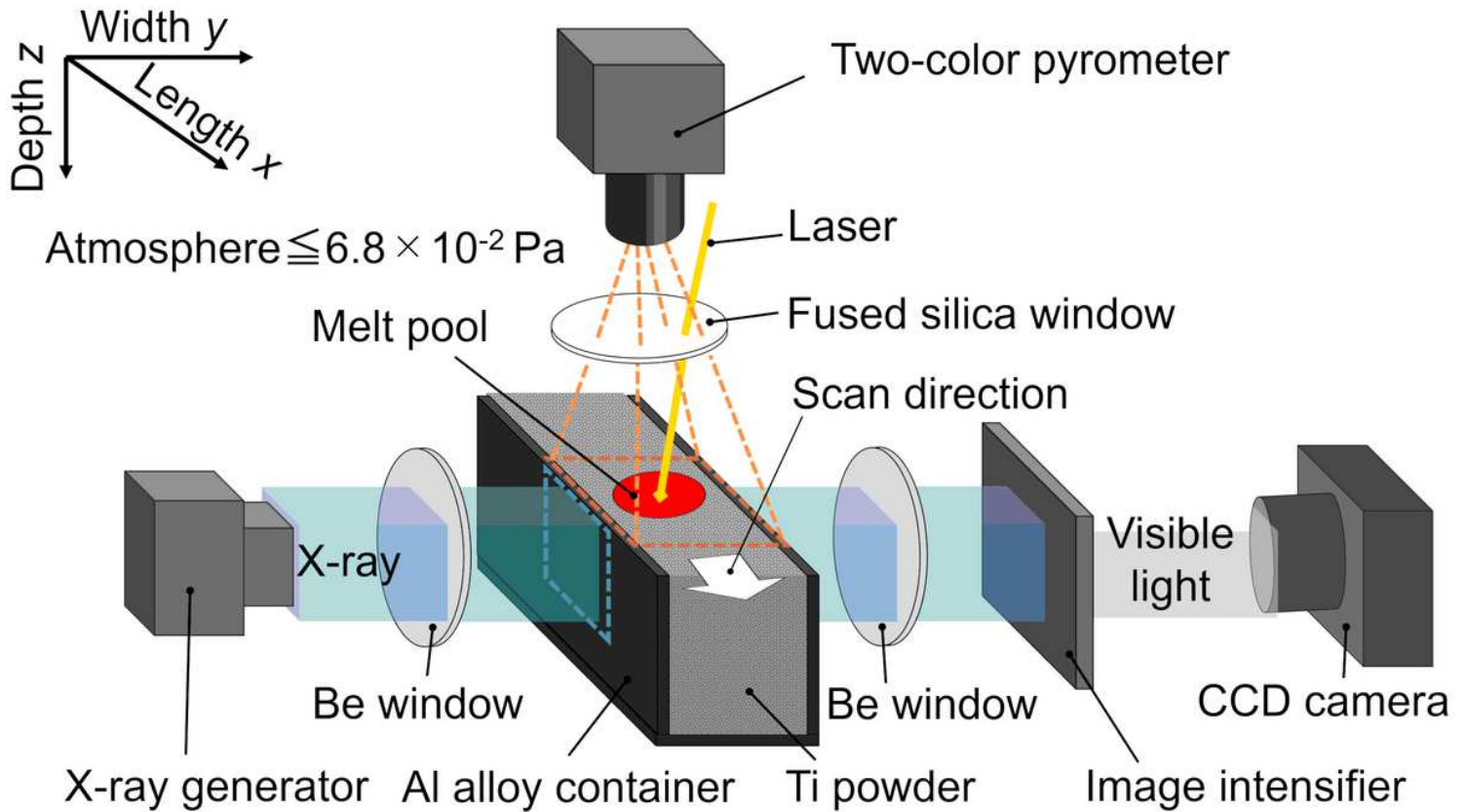


Figure 1

Schematic of LPBF process experiments using X-ray and thermal imaging, and scanning manner.

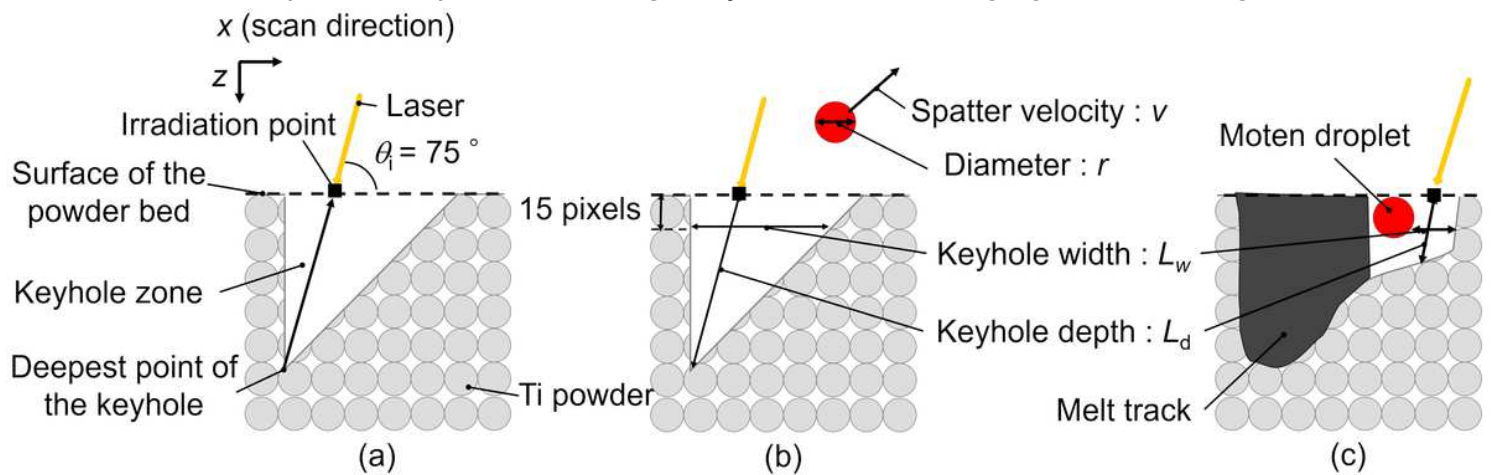


Figure 2

Schematics of cross-sectional views of the powder bed. Definition of each reference point(a), just after laser irradiation start (b), and after generation of the melt track for the definition of measurement points L_w , L_d , v and r (c).

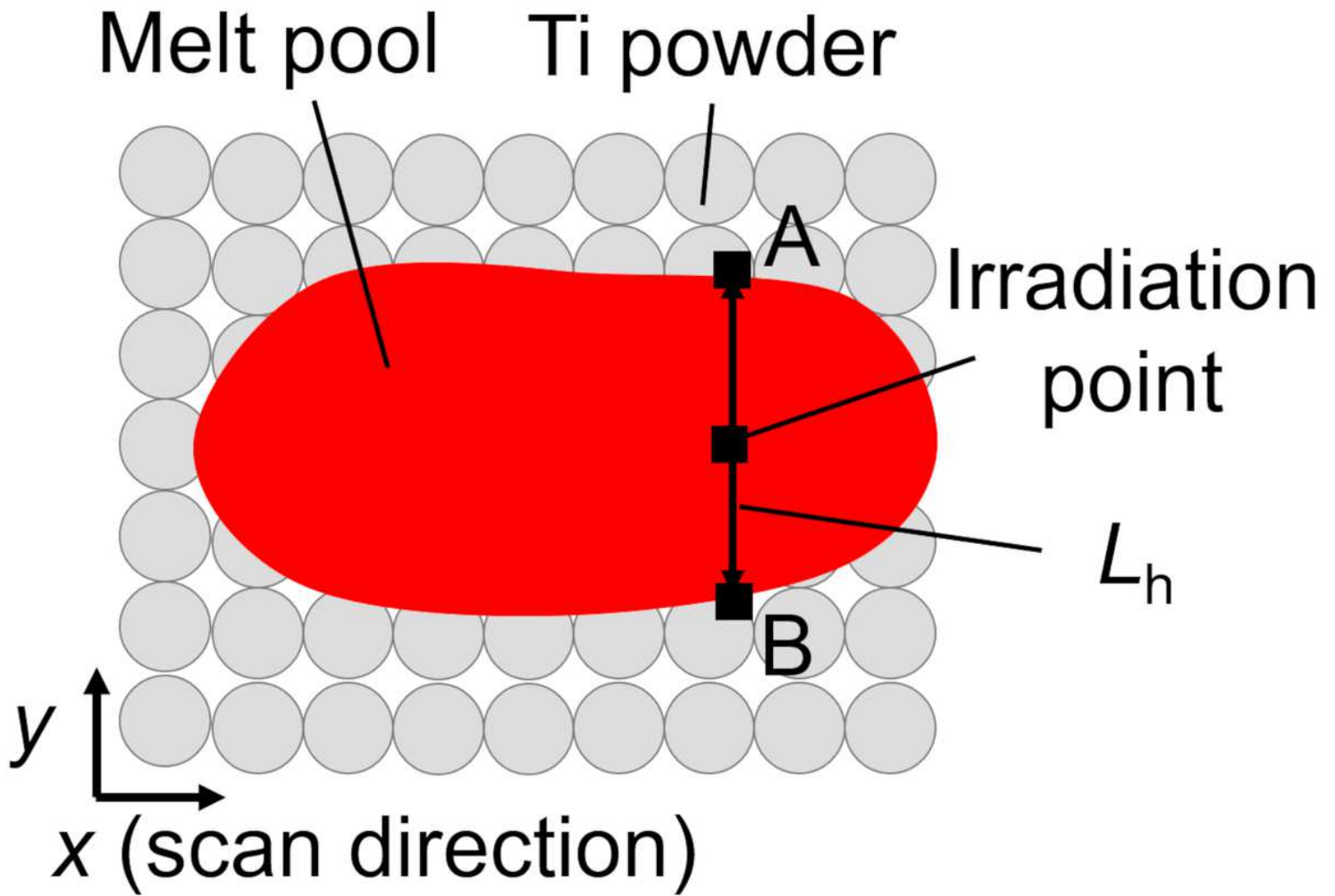


Figure 3

Schematic of the top view of the powder bed for the definition of the high temperature width L_h .
 x (scan direction)

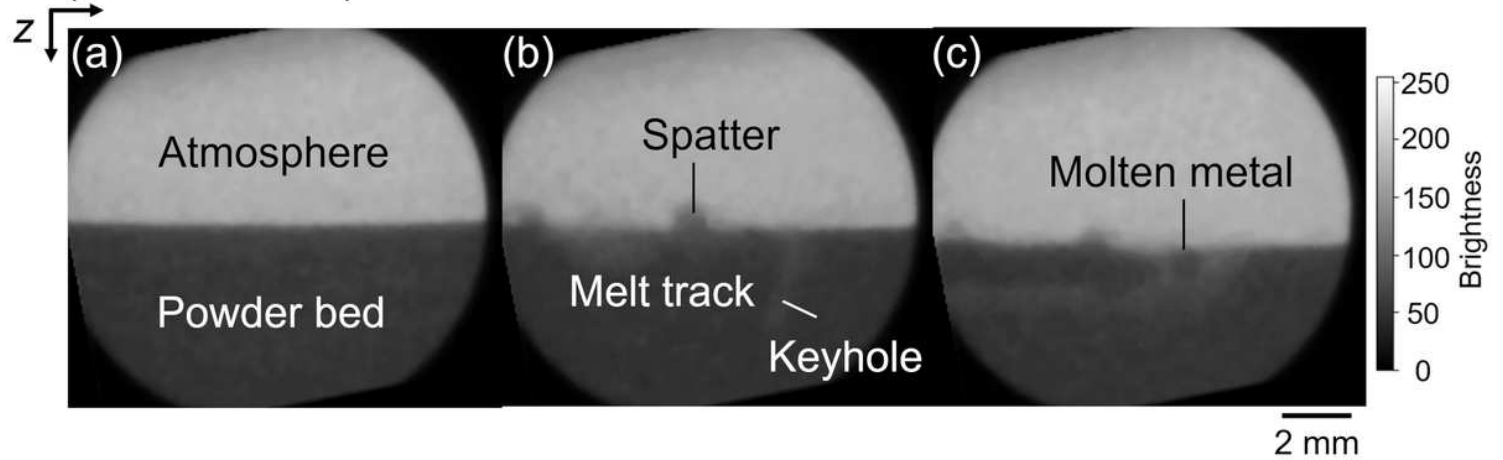


Figure 4

Examples of the obtained raw X-ray images before laser irradiation (a), during laser irradiation at $t = 0.430$ s (b), and during laser irradiation at $t = 2.088$ s (c).

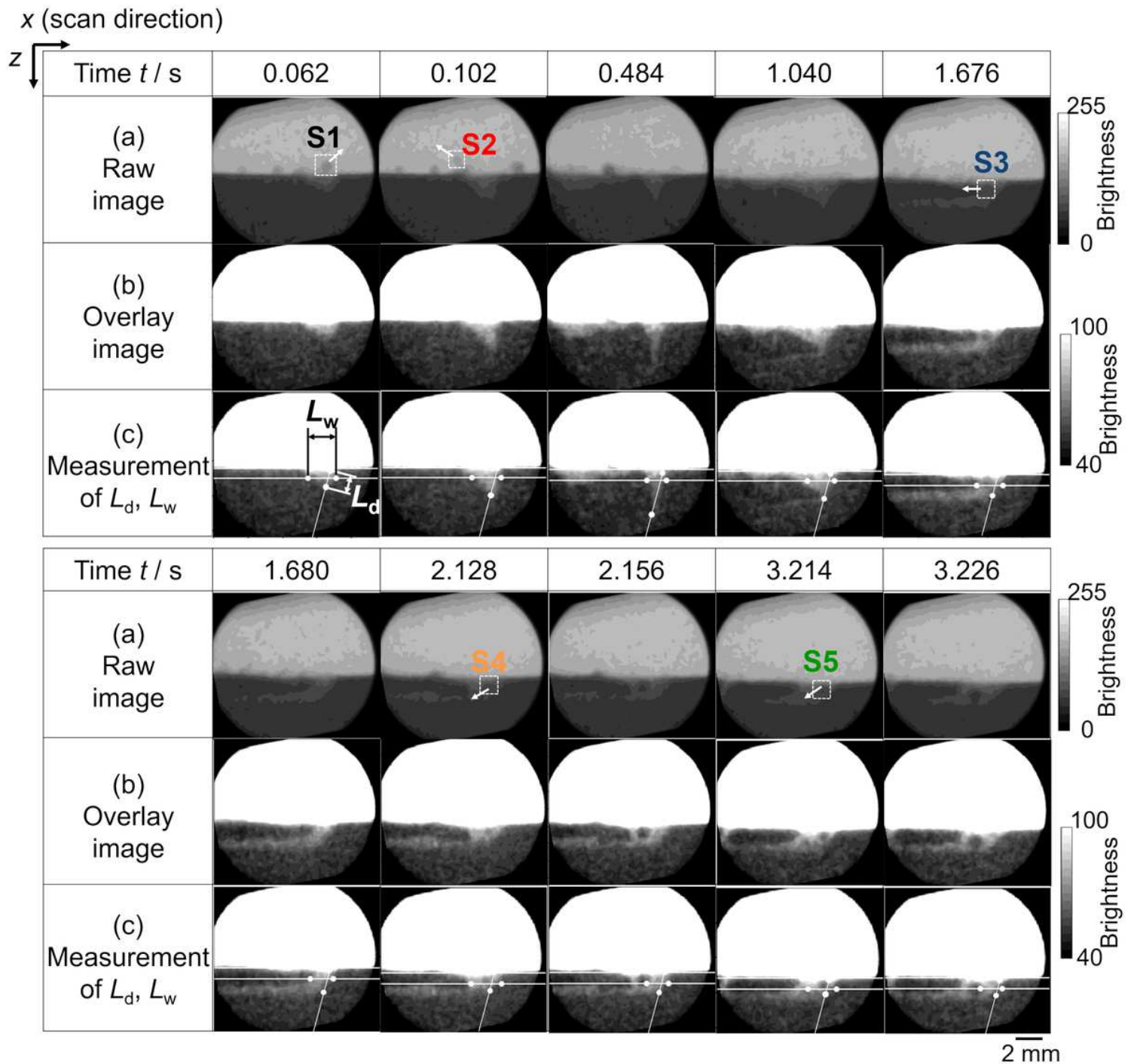


Figure 5

Time change of melting behavior and definition of keyhole depth L_d and keyhole width L_w . Molten droplets named S1~S5 were examples that show characteristic melting behavior. Molten droplets S1 and S2 which were generated just after laser irradiation start were scattered at the direction of the arrow which was shown in Fig5(a). As laser irradiation advanced, molten droplets S3~5 formed right under an irradiation point moved to reverse with the scanning direction.

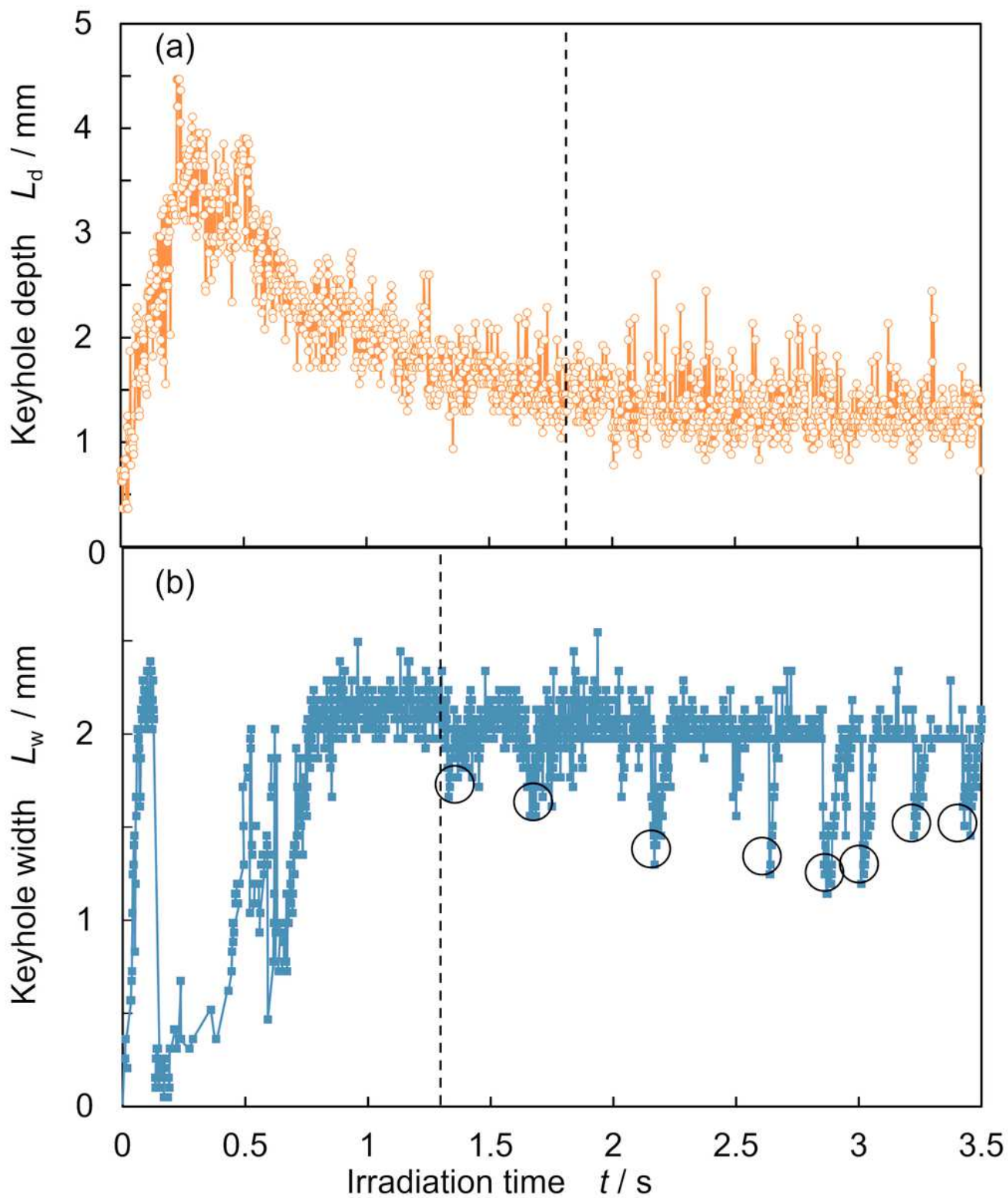


Figure 6

Time variation of keyhole depth L_d (a) and keyhole width L_w (b). The points where the keyhole width was 0 mm were omitted due to the analysis error. The dashed line shows the time when L_d and L_w became constant as shown in chapter 4.1. The circle shows the data which were omitted to calculate the correlation coefficient in chapter 4.1.

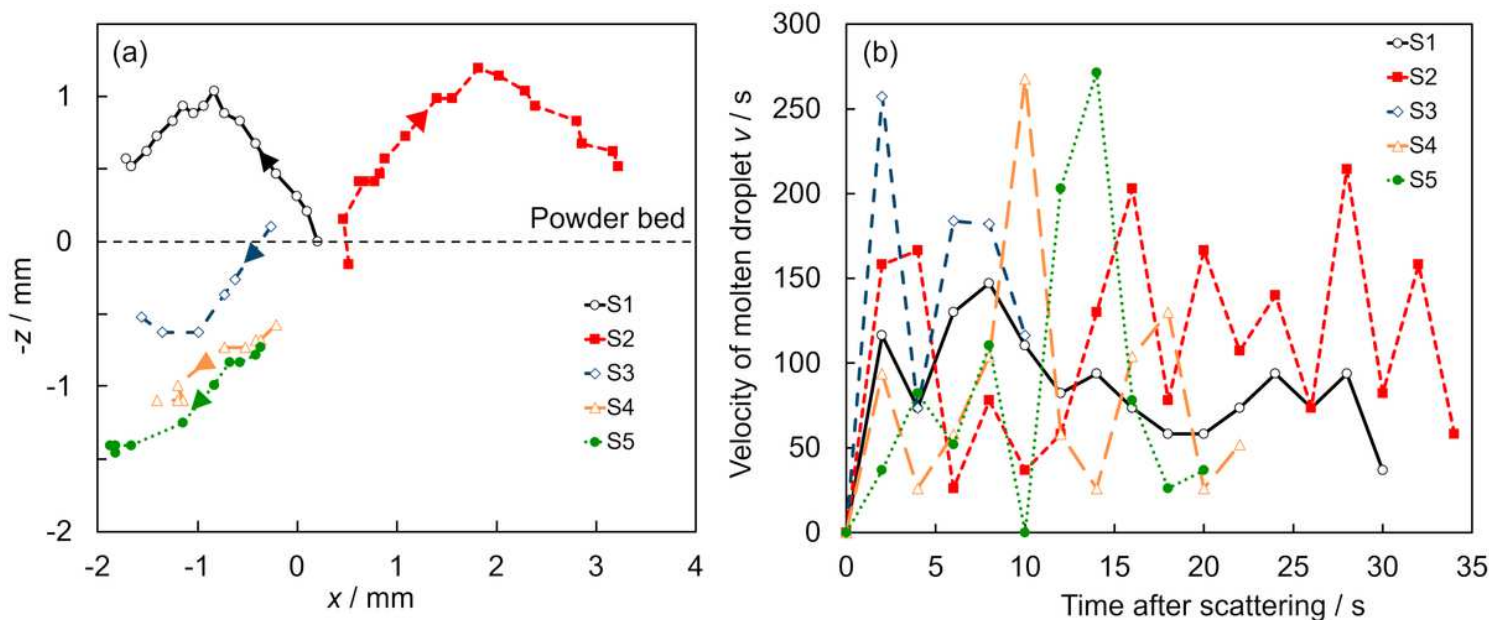


Figure 7

Trajectory (a) and velocity change (b) of molten droplets S1, S2, S3, S4 and S5 shown in Fig5(a). The arrow expresses a scattering direction (a).

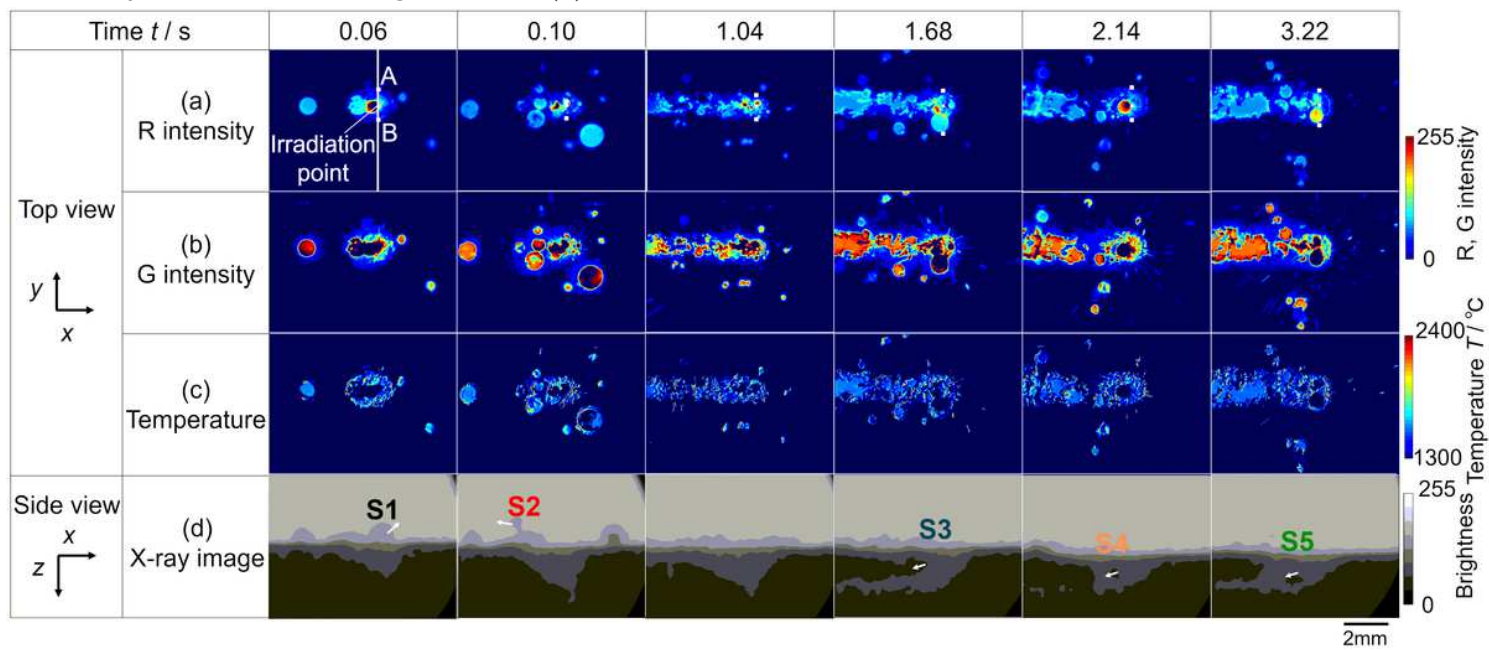


Figure 8

Time change of temperature distribution from the top with corresponding X-ray images from the side. At $t = 0.06$ s in Fig.8(a), the symbols A and B express the edge of the temperature rise area ($R \text{ intensity} \geq 10$) on the straight line that is perpendicular to the x-axis through an irradiation point.

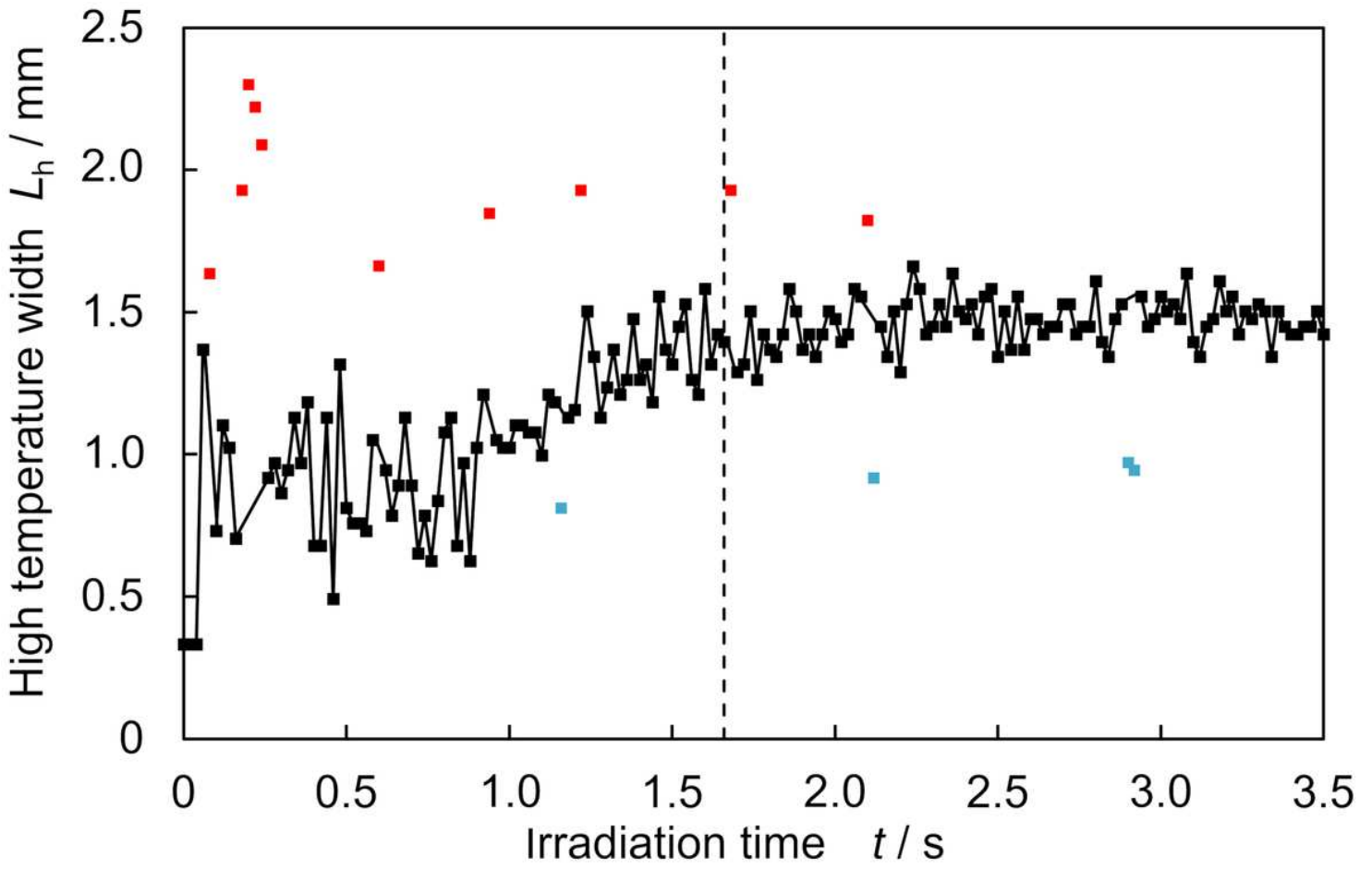


Figure 9

Time change of the high temperature width L_h . The dashed line shows the time when L_h became constant as shown in chapter 4.1. The red plots show that L_h is overestimated by the molten droplet which existed on the measurement line that is parallel to the y-axis through an irradiation point as shown in Figs.10(a) and (b). The light blue plots show that the outline of the temperature rose area could not be extracted because temperature around the irradiation point could not be measured as shown in Figs.10(c).

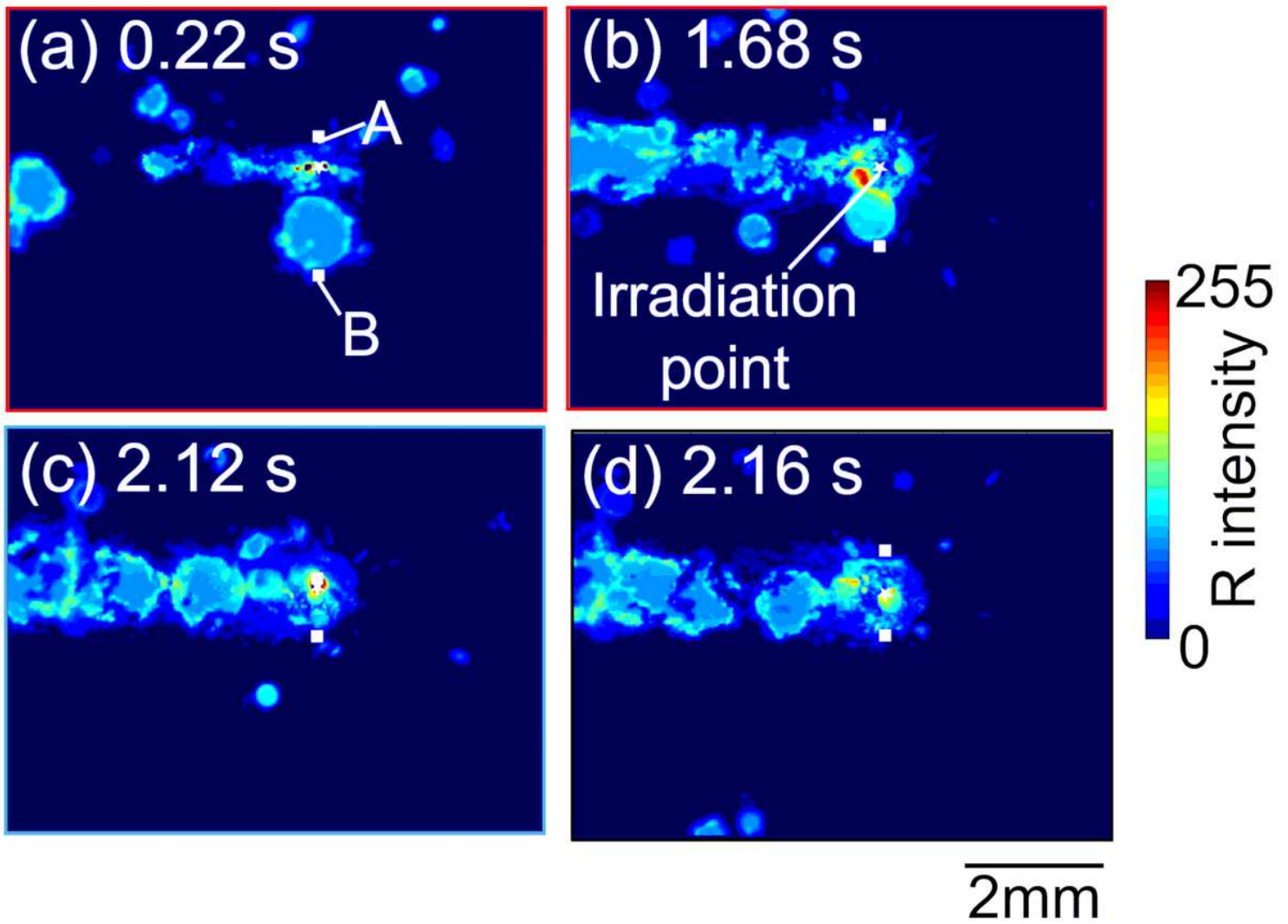


Figure 10

Example of thermal images at each time. The flame color of the images corresponds to the color of the plot in Fig.9. Lh is overestimated by the molten droplet which existed on the measurement line (a), (b). Outline of the temperature rose area could not be extracted because of not measuring temperature around the irradiation point (c). The normal measurement (d)

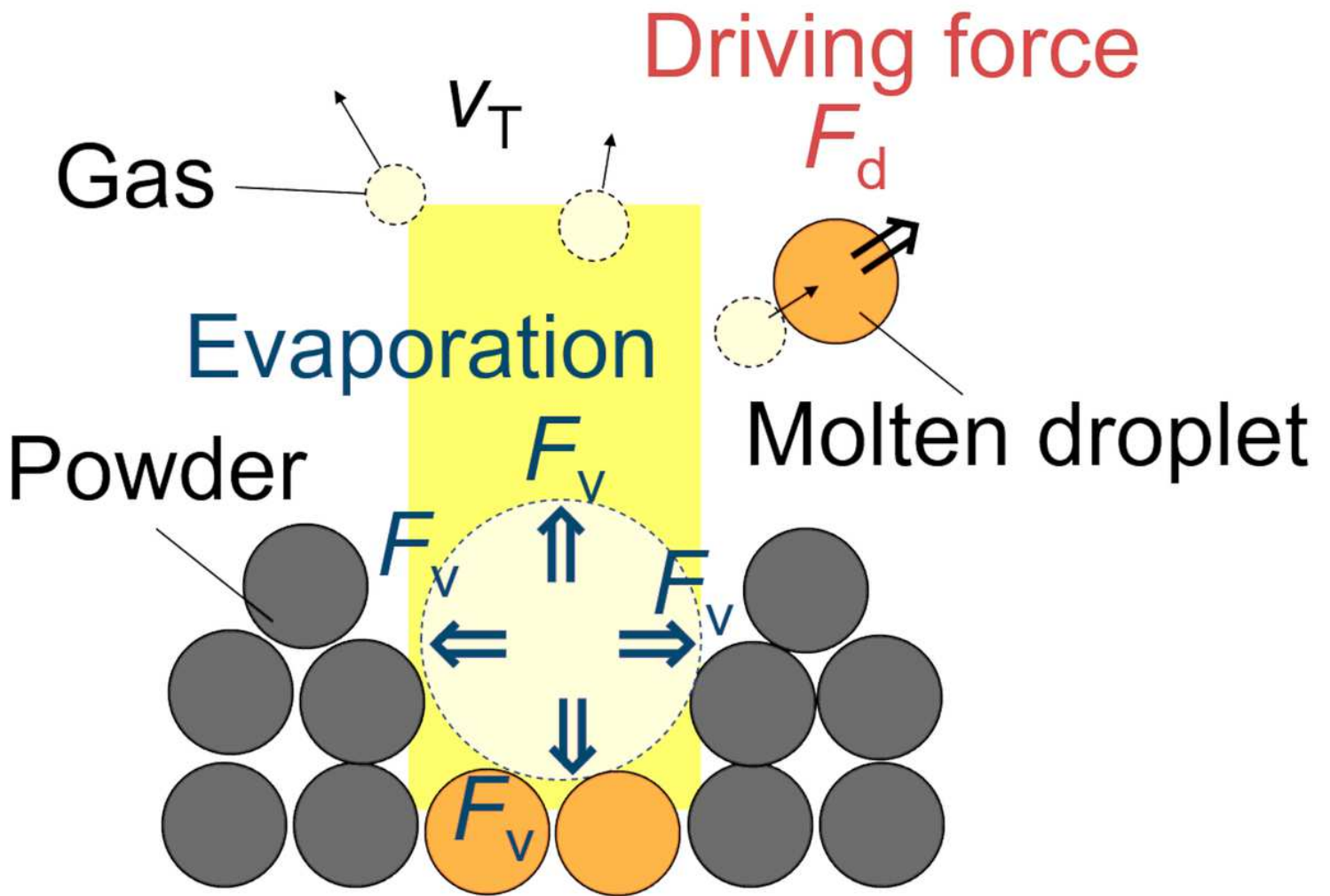


Figure 11

Model of the spattering phenomenon for elucidating the driving force that pushed a molten droplet during the LPBF process.

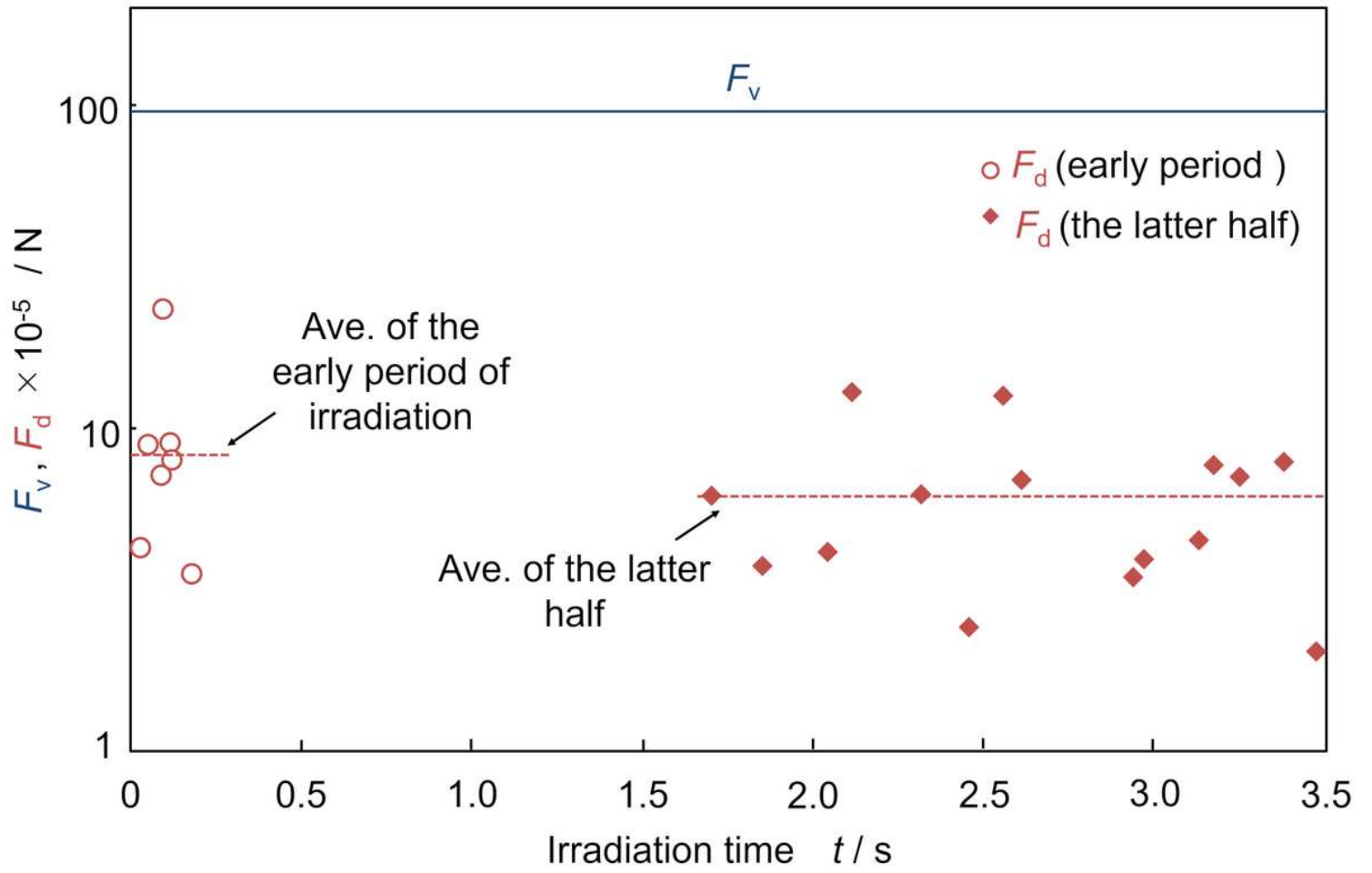


Figure 12

Comparison of the driving force F_d that pushed a molten droplet and vaporization F_v . F_d is the driving force that pushed a molten droplet, F_v is the theoretical value of vaporization.

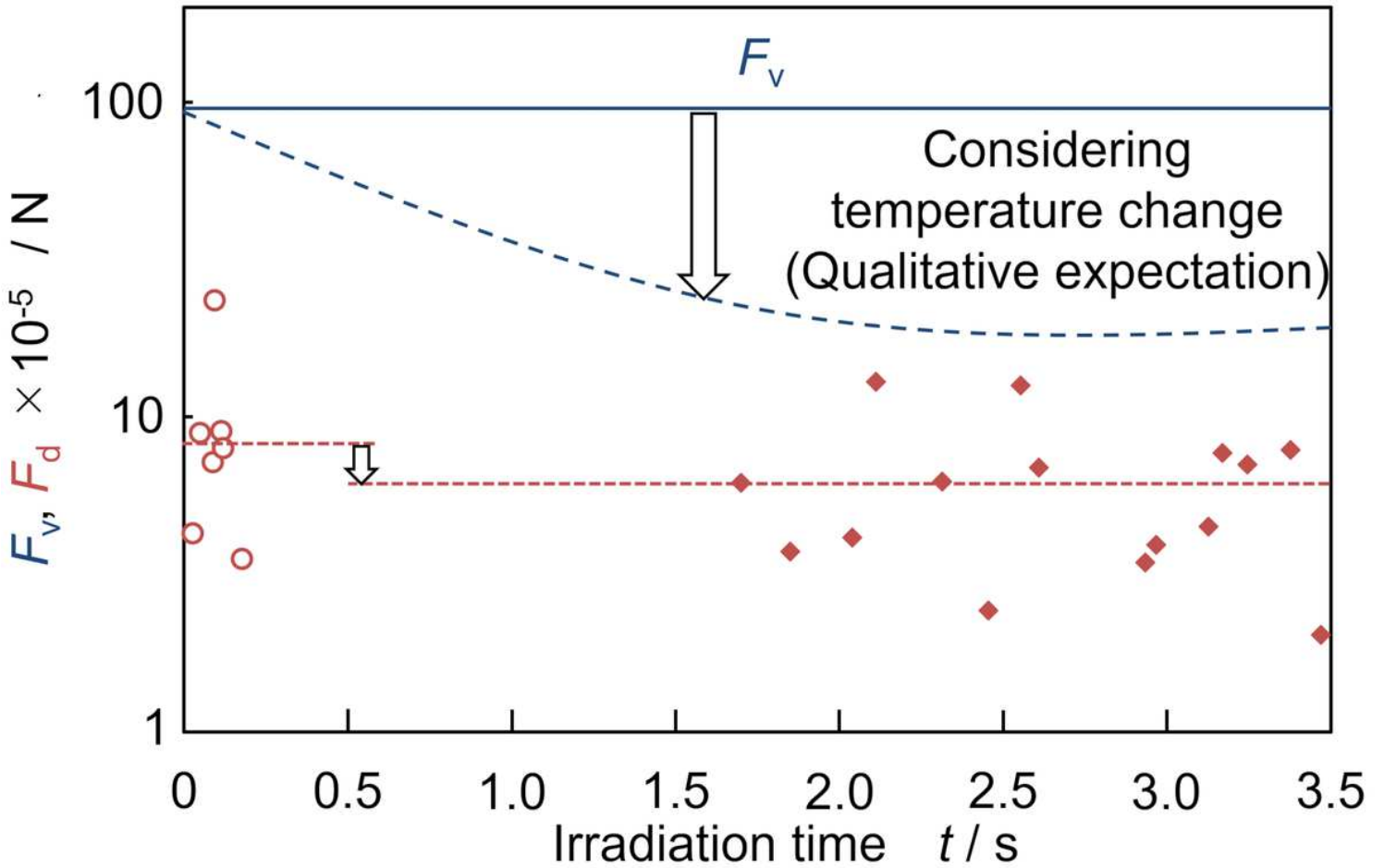


Figure 13

Comparison of the driving force F_d that pushed a molten droplet and vaporization F_v considering temperature change. The schematics that evaporation F_v decreased due to the decrease of quantity of vaporization (m_v) as laser scan advanced. It was thought that as L_h increased, the temperature of the powder metal around the irradiation point rose and sintered material was produced. As a result, thermal diffusion was promoted and local heating was mitigated, and then the quantity of vaporization (m_v) decreased. In addition, the result that the average of the early period of F_d became larger than that of the latter half of F_d was also considered because of the decrease of vaporization.

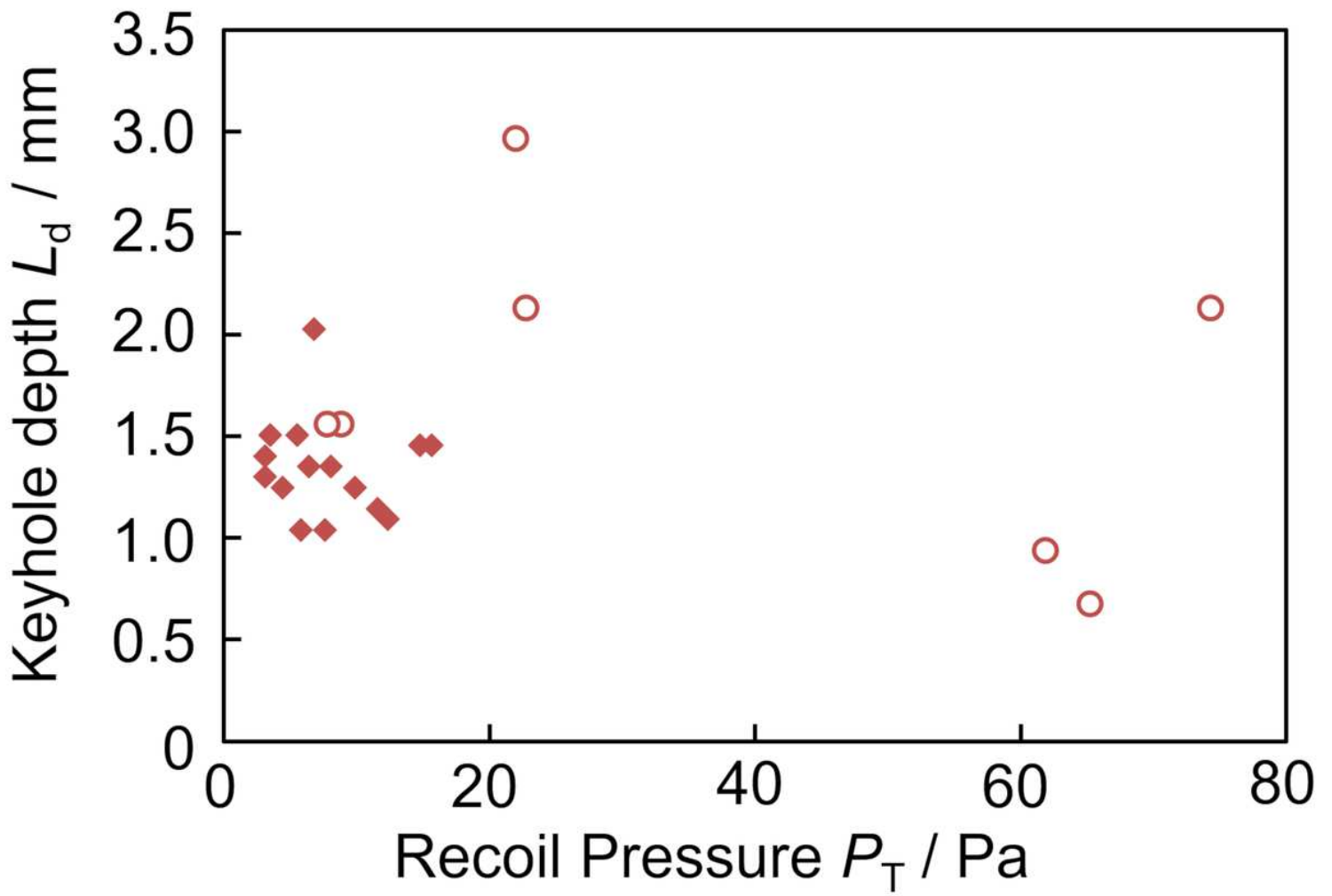


Figure 14

Please see the Manuscript Doc file for the complete figure caption.

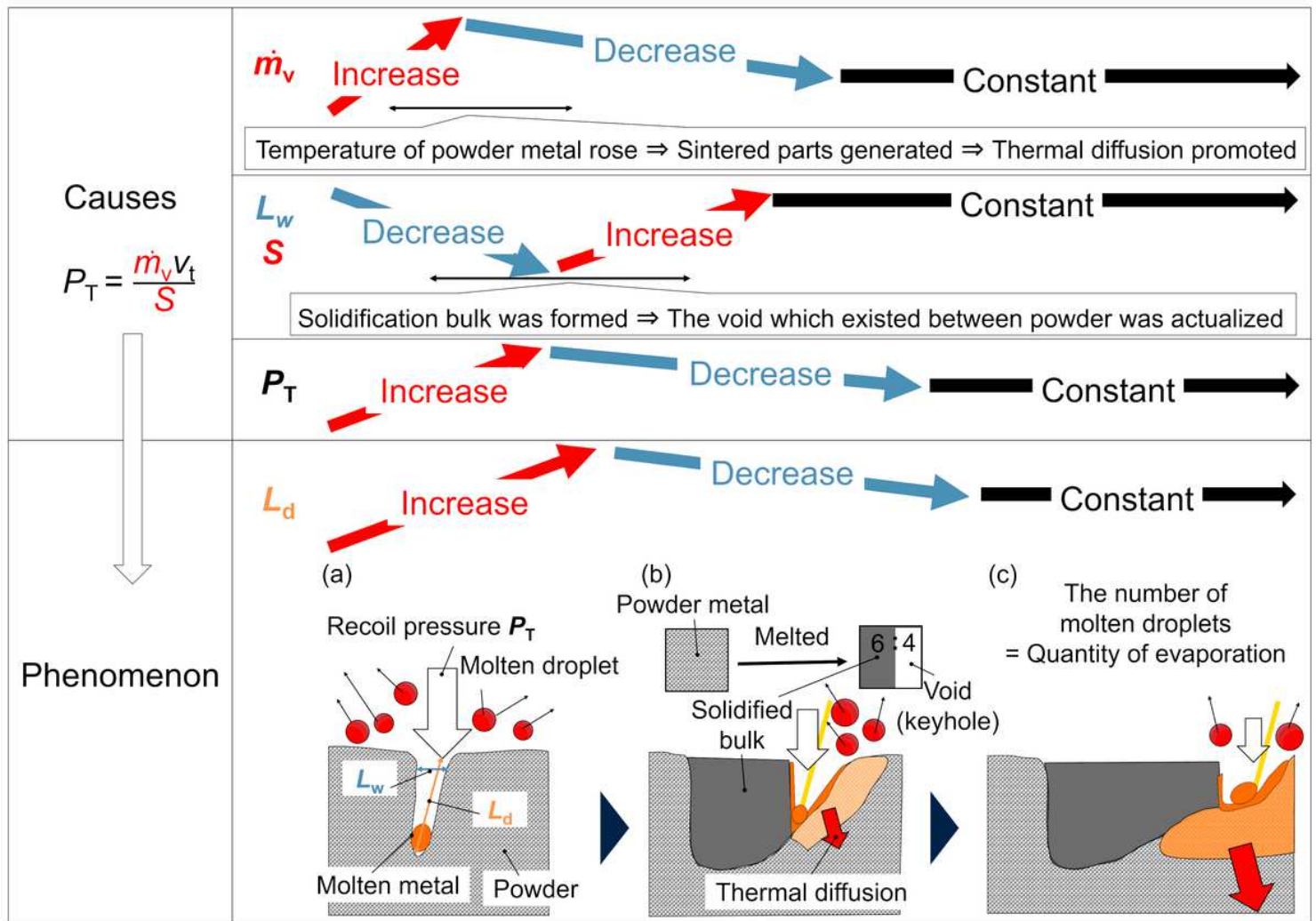


Figure 15

Schematic of the transition mechanism of melt depth by single-track laser irradiation. Keyhole depth L_d increased (a), decreased (b), and became constant (c) in time order. Quantity of vaporization rate (\dot{m}_v) increased immediately after irradiation start, decreased as the laser irradiation advanced, and transitioned to a constant value. The decrease in (\dot{m}_v) can be attributed to the formation of the sintered material, which promotes thermal diffusion and reduces the laser power consumed for evaporation. After $t = 0.13$ s, keyhole width L_w (vaporization area S) decreased once, then increased again and became constant. The increase in L_w considered to be due to the formation of the solidified bulk, which makes the voids between the powder metal apparent. It is assumed that the recoil pressure P_T which is expressed as the ratio of these two parameters (\dot{m}_v and S) increased after the start of laser irradiation, gradually decreased as laser irradiation advanced and then became constant. Due to the causes mentioned above, L_d is thought to have caused the same changes as recoil pressure.

Supplementary Files

This is a list of supplementary files associated with this preprint. [Click to download.](#)

- renamed628be.avi
- Onlinetable1.png